Supplementary Information for Thermal Transport in γ-InSe: Bulk Single Crystals and Thin Flakes

Farjana Ferdous Tonni,[1] Maliha Maliat,[1] Sujit Bati,[2] Md Sabbir Akhanda,[1] Harsh Chandra,[3] Ethan A. Scott,[4] Abir Hasan,[1] Sergiy Krylyuk,[5] Nikhil Shukla,[1] Costel Constantin,[6] Patrick E. Hopkins,[4,7,2] Junichiro Shiomi,[3] Albert V. Davydov,[5] and Mona Zebarjadi[1,7,2]

[1)] *Department of Electrical and Computer Engineering, University of Virginia, Charlottesville, VA 22904, USA*
[2)] *Department of Physics, University of Virginia, Charlottesville, VA 22904, USA*
[3)] *Department of Mechanical Engineering, University of Tokyo, Tokyo 113-8656, Japan*
[4)] *Department of Mechanical and Aerospace Engineering, University of Virginia, Charlottesville, Virginia 22904, USA*
[5)] *Material Science and Engineering Division, National Institute of Standards and Technology, Gaithersburg, MD 20899, USA*
[6)] *Department of Physics and Astronomy, James Madison University, Harrisonburg, Virginia, USA*
[7)] *Department of Materials Science and Engineering, University of Virginia, Charlottesville, VA 22904, USA*

(*Electronic mail: mz6g@virginia.edu)

S1. MATERIAL AND DEVICE FABRICATION

S1.1. Single Crystal Growth and Characterization

InSe single crystals were grown using the vertical Bridgman method. Initially, polycrystalline InSe was synthesized by reacting high-purity In (99.99 %) and Se (99.99 %) in a 52 at. % In to 48 at. % Se ratio in vacuum-sealed quartz ampoules at 720 °C for 8 h in a rocking furnace. The ampoules were graphitized by acetone pyrolysis to prevent selenium from reacting with the quartz. A non-stoichiometric mixture was used based on previous literature, which indicated that an In-rich charge improves the yield of the InSe phase by avoiding peritectic decomposition during the melt cooling process[1]. The resulting poly-InSe was loaded into a new ampoule, which was then sealed under vacuum and placed in a vertical Bridgman furnace. Prior to crystal growth, the InSe charge was maintained at 720 °C for 3 h to achieve melt homogenization. The molten charge was then moved through a thermal gradient at a rate of 0.5 mm/h. To obtain n-type doped InSe crystals, Sn (5 at. %) was added to the In:Se mixture during polycrystalline InSe synthesis. This resulted in the production of InSe ingots with a length of 4 cm and a diameter of 1 cm. Building on the previously reported structural and electrical characterization of the samples (XRD, ADF-STEM, and Hall measurements)[2–4], we first assessed the compositional uniformity using SEM–EDX analysis. The elemental mapping confirms the uniform spatial distribution of indium (In) and selenium (Se) across the scanned area. The absence of noticeable compositional segregation or clustering indicates good chemical homogeneity of the sample, suggesting stoichiometric and phase-uniform InSe within the probed region as shown in Fig. S1.

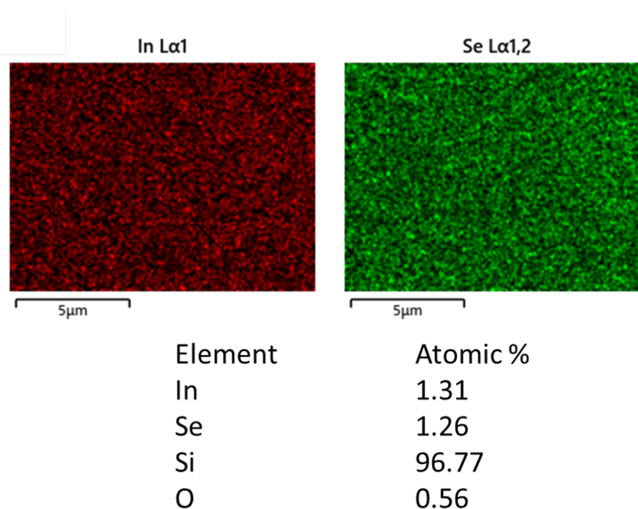

FIG. S1. SEM-EDX scan representing uniform distribution of In and Se atoms.

Two single-crystal bulk samples studied here were cleaved from the respective ingots using a razor blade and used without further processing. The preparation method, therefore, is at least partially responsible for the observed surface roughness. Fig. S2 provides additional optical and three-dimensional surface profilometry images of the cleaved n-type InSe bulk crystals discussed in the main text. The profilometry maps highlight the surface roughness and lateral thickness nonuniformity across the crystal surfaces, which underline the thickness variations and associated uncertainties reported in the main text.

S1.2. 2D Device Fabrication

Thin γ-InSe flakes were mechanically exfoliated from bulk crystals onto pre-cleaned 300 nm SiO_2/p^+-Si substrates using adhesive tape (SPV 224PR-MJ, PVC-based surface pro-

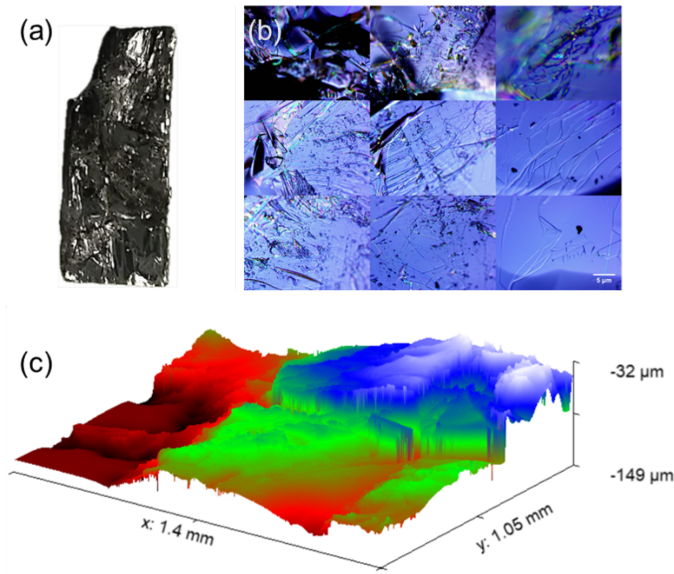

FIG. S2. (a) Bulk single crystal of n-type InSe, (b) Optical images of the surface of bulk n-type InSe; Inset: zoomed-out image showing the full extent of the sample, (c) 3D image of the surface roughness generated by Optical Surface Profiler.

tective tape). The choice of substrate is dictated by the requirements of the thermal conductivity measurements. We employ heat diffusion imaging, which is based on the original heat spreader method. In this technique, the film of interest (InSe) should possess a higher in-plane thermal conductivity than the supporting layer. Therefore, it should be supported by a thin insulating layer (300 nm SiO_2) on a high–thermal conductivity substrate that serves as a heat sink or isothermal substrate (p^+-Si)[5]. Substrates were cleaned by sequential sonication in acetone and isopropyl alcohol, drying with N_2, and a final UV–ozone treatment. Flakes with lateral dimensions larger than 15 μm $\times$ 20 μm were used for two devices, while a flake with lateral dimensions of 6 μm $\times$ 20 μm was used for a third device. Representative AFM topography images of both intrinsic and doped flakes are shown in Fig. S3. Thinner flakes generally exhibit lower surface roughness; in addition, the doped flakes studied here show smaller roughness values compared to the intrinsic flakes.

Fig. S4 shows an optical microscopy image of representative exfoliated flakes. Two-dimensional devices were subsequently fabricated by depositing metal lines (heater) on the sample for in-plane thermal conductivity measurements. Initially, the heater/electrode pattern was prepared using Quantum Design MicroWriter ML3 Pro direct-write laser lithography (385 nm). 10 nm Ti and 190 nm Ni were evaporated as contact metals (base pressure $\approx$ 1 mPa) at a deposition rate 0.5 Å s^{-1} for Ti and 1.0 Å s^{-1} for Ni. The samples were annealed under high vacuum ($\approx$0.1 mPa) at 300 °C for 30 min in the cryostat immediately before measurements to minimize the effects of environmental contamination during the fabrication processes.

After the thermal transport measurements, the thicknesses

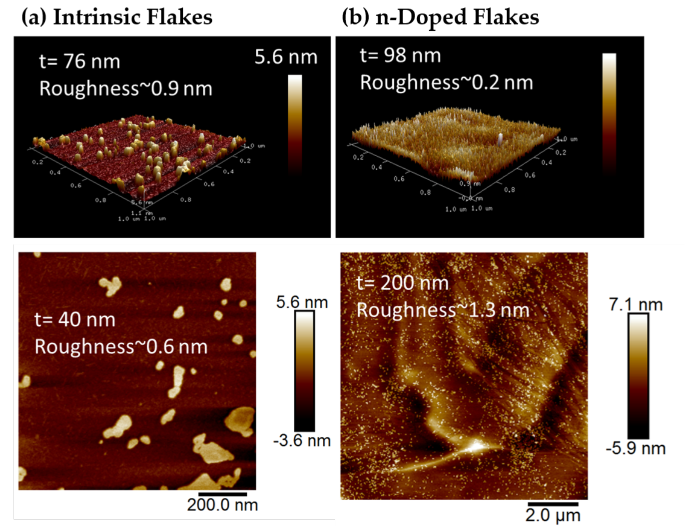

FIG. S3. Atomic Force Microscopy (AFM) image of representative (a) intrinsic and (b) doped flakes.

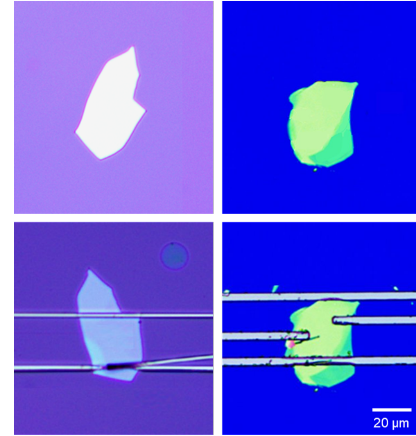

FIG. S4. Optical microscopy images of the exfoliated flakes (upper panel) and fabricated devices (lower panel) used for thermal transport measurements.

of the exfoliated InSe flakes were measured using a Tencor P-7 stylus profiler. The measurements were performed last to minimize exposure to the environment, preventing contamination that could alter the thermal conductivity values. Fig. S5 shows the thickness profile of one representative device out of the three measured. The profile illustrates the local flake thickness and any surface variation. The other two devices exhibited similar thicknesses and uniformity, confirming that the measured flakes are representative of the samples used for thermal conductivity analysis.

S2. MEASUREMENT METHOD, APPLICABILITY AND VALIDATION

We measured the cross-plane thermal conductivity of InSe flakes using time-domain thermoreflectance (TDTR). We uti-

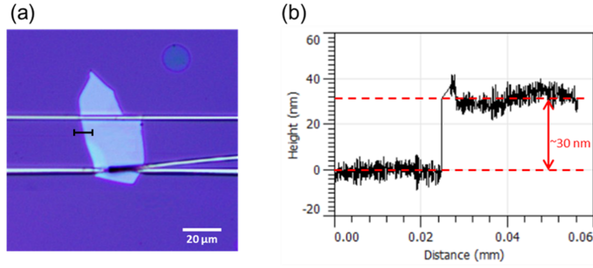

FIG. S5. Thickness measurement from Stylus Profiler. (a) Optical image and (b) step profile of the 30nm thick sample for thermal transport measurement.

lized a Ti:Sapphire laser to produce a pulsed beam with a central wavelength of 808 nm, full width at half-maximum of 13 nm, and a pulse width of 150 fs. A two-tint configuration[6]. is employed to separate the beam into pump and probe paths spectrally. The pump is amplitude-modulated with an electro-optic modulator at a frequency of 8.4 MHz. The probe pulses are time-delayed, up to 5.5 ns relative to the pump, with an optical delay line. The two beams are made colinear with a dichroic mirror and focused upon the sample surface with an objective lens, which results in $1/e^2$ diameters of 11 μm and 19 μm for the probe and pump, respectively. The sample was coated with 95 nm of aluminum prior to measurement with TDTR. We then measured the sample off-flake to obtain the thermal conductivity of the 300 nm oxide layer. We assume a value of 1.63 $MJm^{-3}K^{-1}$[7]. for the heat capacity, and fit the TDTR data (ratio of in-phase and out-of-phase signals from the lock-in amplifier) and obtained a thermal conductivity of (1.33 $\pm$ 0.9) $Wm^{-1}K^{-1}$. The oxide thickness was sufficiently thick such that sensitivity to the properties of the underlying silicon substrate was minimal. Measurements were subsequently performed on the InSe flake. To analyze the thermoreflectance data, we assume a heat capacity of 1.3 $MJm^{-3}K^{-1}$[8] and apply the in-plane thermal conductivity obtained from the electro-thermal measurement. The thermal boundary conductance between the Al/InSe and InSe/SiO2 interfaces is unknown. However, we find that the resultant cross-plane thermal conductivity varies approximately 10 % in response to an order of magnitude change in the assumption (100 $MWm^{-2}K^{-1}$ to 1000 $MWm^{-2}K^{-1}$). We therefore fit the data at the extremes of this range and take the average value. With this approach, we obtain a cross-plane thermal conductivity of (0.37 $\pm$ 0.06) $Wm^{-1}K^{-1}$, where the uncertainty accounts for the variance in measurement repeatability as well as uncertainty in the interface conductance on either side of the film. For the case of an intrinsic sample, a flake was placed on a silicon substrate. A modulation frequency of 11.05 MHz was used, and interfacial thermal boundary conductances of 50 $MWm^{-2}K^{-1}$ and 20 $Wm^{-2}K^{-1}$ were assumed to provide the best fit result for the cross-plane thermal conductivity.

In-plane Thermal transport measurements on the flakes were performed using the Heat Diffusion Imaging (HDI) technique[9] in the in-plane direction. The HDI method is a hybrid method that combines thermoreflectance imaging system

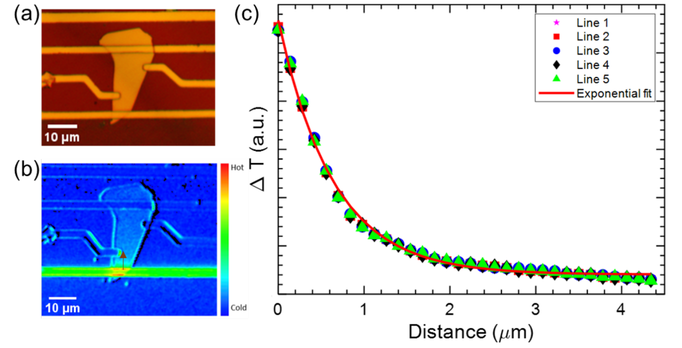

FIG. S6. (a) Optical image of an InSe device for thermal transport measurement (b) Thermoreflectance map of the sample surface with a 3V bias applied to the heater. Temperature decay curves were taken along the sample perpendicular to the heater. (c) Temperature decay curves and their corresponding exponential fit for thermal conductivity extraction

to capture the temperature decay along the sample after a heat flow is injected through a heater attached to the edge of the sample, and the heat spreader method to analyze and extract the thermal conductivity from the details of the temperature decay along the sample. The concept of the heat spreader has been successfully applied to 2D systems as thin as a few layers, demonstrating its effectiveness in such thin materials[10–13]. This technique enables spatially resolved measurement of in-plane thermal conductivity while minimizing sample damage or contamination, making it particularly suitable for delicate 2D materials. Therefore, it has been successfully applied to measure in-plane thermal conductivity of 2D materials with thicknesses comparable to our InSe flakes (30 nm), including $NbSe_2$, $MoTe_2$, and $PtSe_2$[11–13]. These studies demonstrate that HDI can be reliably used to study intrinsic thermal transport in few-layer systems.

The thermoreflectance imaging system used in the HDI technique exploits the fact that the surface reflectivity, R, of a material varies with temperature, T. This relation is expressed as $\Delta T = \Delta R / C_{TR} R$, where C_{TR} is the thermoreflectance coefficient. C_{TR} depends primarily on the material surface, the ambient temperature, and the illumination wavelength. In principle, C_{TR} must be known to determine absolute surface temperatures; however, absolute temperature calibration is not required for the extraction of in-plane thermal conductivity in the HDI method. This is because $\kappa_{\parallel}$ is determined from the spatial decay rate of the temperature profile rather than from its absolute magnitude, as described below.

A representative temperature profile along the flake is shown in Fig. S6. The temperature decay along the x-axis perpendicular to the heater is exponential and described by $\exp(-\beta x)$, where $\beta = \sqrt{k_i/(k_x d_i d)}$. Here, k_i is the cross-plane thermal conductivity of the insulating layer, d_i is its thickness, d is the thickness of the target film, and k_x is its in-plane thermal conductivity being extracted. The characteristic decay length $1/\beta$, obtained from an exponential fit to the measured temperature profile, is thus the key metric for determining $\kappa_{\parallel}$. In this fin-type model, heat leakage through

the substrate is accounted for via the thermal resistance of the insulating layer, which enters directly into the evaluation of β.

Measurements were performed using a 470 nm blue LED as the illumination source. Electrical pulses of 3 to 5 V amplitude and 5 ms duration were applied to the Ni heater at a 20% duty cycle. The thermoreflectance map shown in Fig. S6 is averaged over several hundred thermal excitation cycles and acquired under 60x magnification. Since β depends only on the rate of spatial temperature decay and not on absolute temperature values, calibration of C_{TR} is not required to extract $\kappa_{\parallel}$. The Ni heater line serves as the reference material: the thermoreflectance coefficient of Ni under 470 nm illumination is known from the literature[14], enabling us to monitor the heater temperature rise and confirm that it remains below 50 K throughout all measurements. This ensures that the single-C_{TR} assumption across the heater remains valid, and the associated temperature uncertainty is included in the reported error bars.

In the HDI method, it is necessary to separate the target film and the heat sink by an insulating layer. Here we use a SiO_2/Si substrate, in which the bottom silicon layer acts as a heat sink, and the top SiO_2 layer serves as the insulating layer. The thermal conductivity of SiO_2 is reported to be less than 1.4 $Wm^{-1}K^{-1}$ across the measured temperature range[15], which ensures a high thermal resistance of the cross-plane and allows accurate measurements of the thermal conductivity of the sample when it is larger than a few $Wm^{-1}K^{-1}$.The uncertainties in the reported thermal conductivity values arise primarily from an estimated 2% error in the sample temperature, which also affects the referenced SiO_2 thermal conductivity, as well as variations in the extracted values of the decay constant. To ensure reproducibility, the temperature decay was measured over 5-10 lines perpendicular to the heater line (see Fig. 3 in the main text) across multiple thermal images. Thermal conductivity was extracted individually for each line and each image, and the average over all measurements was reported. The standard deviation of these values is presented as the error bar, reflecting both the measurement reproducibility and the intrinsic experimental uncertainty.

S3. SENSITIVITY OF THERMAL CONDUCTIVITY CALCULATIONS TO ROUGHNESS

In the Callaway model, surface roughness enters through a frequency-dependent specularity parameter $p(\omega) = \exp(-4\eta_{\mathrm{rms}}^2\omega^2/v_s^2)$, which interpolates between specular ($p = 1$) and fully diffuse ($p = 0$) boundary scattering. For the bulk crystals, optical profilometry confirms that the surface roughness is sufficiently large to place the boundary scattering in the fully diffusive limit, where $\tau_b^{-1} = v_s/L$, and the thermal conductivity is insensitive to further variations in roughness.

For the exfoliated flakes, AFM measurements (Fig. S3) indicate nanometer-scale RMS roughness. Figure S7 shows the calculated in-plane thermal conductivity of the n-doped flake as a function of η_{rms}. As η_{rms} increases from zero, $\kappa_{\parallel}$ decreases rapidly, reflecting the transition from specular to diffuse boundary scattering. Once η_{rms} approaches $\sim$1 nm — consistent with the experimentally observed roughness — the calculated $\kappa_{\parallel}$ approaches the diffuse limit and becomes effectively insensitive to further increases in roughness. Within the physically realistic roughness range of our samples, boundary scattering is therefore near saturation, and variations in η_{rms} do not significantly alter the extracted $\kappa_{\parallel}(T)$.

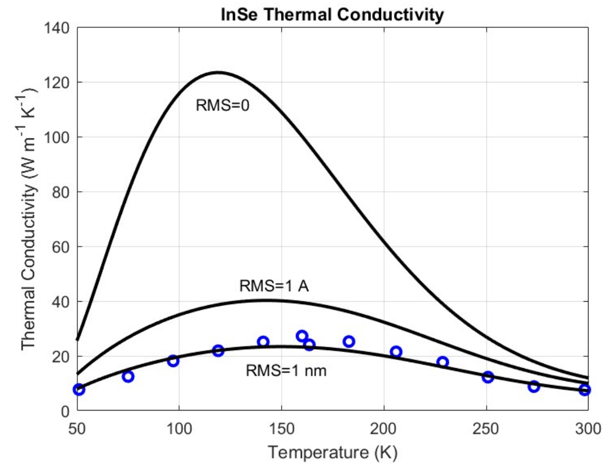

FIG. S7. Roughness sensitivity analysis for doped-flake. The η_{rms} values are changed from 0 (specular) to 1 nm (diffusive). Further increase of roughness does not affect the results significantly.

[1] A. Chevy, A. Kuhn, and M.-S. Martin, "Large inse monocrystals grown from a non-stoichiometric melt," J. Cryst. Growth **38**, 118 (1977).

[2] J. Miao, C. Leblanc, J. Wang, Y. Gu, X. Liu, B. Song, H. Zhang, S. Krylyuk, W. Hu, A. V. Davydov, T. Back, N. Glavin, and D. Jariwala, "Heterojunction tunnel triodes based on two-dimensional metal selenide and three-dimensional silicon," Nature Electronics **5**, 744 (2022).

[3] C. Patil, C. Dong, H. Wang, B. M. Nouri, S. Krylyuk, H. Zhang, A. V. Davydov, H. Dalir, and V. J. Sorger, "Self-driven highly responsive p-n junction inse heterostructure near-infrared light detector," Photonics Res. **10**, A97 (2022).

[4] N. A. Pike, R. Pachter, M. A. Altvater, C. E. Stevens, M. Klein, J. R. Hendrickson, H. Zhang, S. Krylyuk, A. V. Davydov, and N. R. Glavin, "Understanding the origin and implication of the indirect-to-direct bandgap transition in multilayer inse," J. Phys. Chem. C **128**, 7957 (2024).

[5] C. Dames, "MEASURING THE THERMAL CONDUCTIVITY OF THIN FILMS: 3 OMEGA AND RELATED ELECTROTHERMAL METHODS," Annual Review of Heat Transfer **16**, 7–49 (2013).

[6] K. Kang, Y. K. Koh, C. Chiritescu, X. Zheng, and D. G. Cahill, "Two-tint pump-probe measurements using a femtosecond laser oscillator and sharp-edged optical filters," Review of Scientific Instruments **79**, 114901 (2008).

[7] E. Ziade, "Wide bandwidth frequency-domain thermoreflectance: Volumetric heat capacity, anisotropic thermal conductivity, and thickness measurements," Review of Scientific Instruments **91**, 124901 (2020).

[8] A. Rai, V. K. Sangwan, J. T. Gish, M. C. Hersam, and D. G. Cahill, "Anisotropic thermal conductivity of layered indium selenide," Applied Physics Letters **118** (2021), 10.1063/5.0042091.

[9] T. Zhu, D. H. Olson, P. E. Hopkins, and M. Zebarjadi, "Heat diffusion imaging: In-plane thermal conductivity measurement of thin films in a broad temperature range," Review of Scientific Instruments **91** (2020), 10.1063/5.0024476, arXiv:2004.07428.

[10] W. Jang, Z. Chen, W. Bao, C. N. Lau, and C. Dames, "Thickness-dependent thermal conductivity of encased graphene and ultrathin graphite," Nano Letters **8**, 4123–4128 (2008).

[11] T. Zhu, P. Litwin, M. G. Rosul, D. Jessup, M. S. Akhanda, F. Tonni, S. Kry-

lyuk, A. Davydov, P. Reinke, S. McDonnell, and M. Zebarjadi, "Transport properties of few-layer nbse2: From electronic structure to thermoelectric properties," Materials Today Physics **27**, 100789 (2022).

[12]T. Zhu, S. S. Das, S. N. Sadeghi, F. F. Tonni, S. Krylyuk, C. Constantin, K. Esfarjani, A. V. Davydov, and M. Zebarjadi, "Electrostatic modulation of thermoelectric transport properties of 2H–$MoTe_2$," Energy Advances (2023), 10.1039/D3YA00316G.

[13]J.-M. Cho, W.-Y. Lee, F. F. Tonni, M.-J. Kim, Y.-H. Kim, H. J. Kwon, J.-W. Choi, M. Zebarjadi, N.-W. Park, S. S. Das, G.-S. Kim, and S.-K. Lee, "Anomalous thermal transport of vertically stacked ptse2 thin films with interface formation," J. Mater. Chem. A **12**, 18348–18357 (2024).

[14]P. Komarov, M. Burzo, and P. Raad, "A thermoreflectance thermography system for measuring the transient surface temperature field of activated electronic devices," in *Twenty-Second Annual IEEE Semiconductor Thermal Measurement And Management Symposium* (2006) pp. 199–203.

[15]Y. S. Touloukian, R. W. Powel, C. Y. Ho, and P. G. Klemens, "Thermal conductivity of nonmetallic solids," Thermophysical Properties of Matter **2**, 1389 (1970).